PHYSICAL REVIEW B VOLUME 62, NUMBER 15 15 OCTOBER 2000-I

Surface potential at surface-interface junctions in $SrTiO_3$ bicrystals

Sergei V. Kalinin and Dawn A. Bonnell*
Department of Materials Science and Engineering, The University of Pennsylvania, 3231 Walnut Street, Philadelphia, Pennsylvania 19104
(Received 3 April 2000)

An analytical approach to the quantification of electrostatic force microscopy and scanning surface potential microscopy images of systems with electric potential inhomogeneity has been developed in order to determine the interface potential in a donor-doped $\Sigma 5$ $SrTiO_3$ grain boundary. The voltage dependencies of the electrostatic force gradient and surface potential verify the solutions. The distance dependencies of force gradient and surface potential were used to quantify the potential at the grain boundary-surface junction and the depletion width. Both measurements yield the same properties despite the difference in imaging mechanisms. The interface potential is shown to result from local charge rather than from a local variation in dielectric constant. The amount of charge implied by an interface potential of 30 mV would render detection of associated defects impossible, but these results represent a lower limit in intrinsic bulk grain boundary potential.

I. INTRODUCTION

Perovskite-based oxide materials are widely used for many commercial applications in conjunction with semiconducting,[1] ferroelectric,[2,3] superconducting,[4] and magnetoresistive[5] properties. The macroscopic properties of perovskite ceramics are largely determined by the microstructure, particularly by grain boundary structure and topology. Very often grain boundaries give rise to useful properties, such as low-field magnetoresistance,[6] positive temperature coefficient of resistivity (PTCR),[7,8] and varistor behavior.[9] The perovskite $SrTiO_3$ is a prototype of oxides in which the presence of interface charge due to intrinsic grain boundary states, or impurity and/or vacancy segregation results in the formation of Schottky barriers similar to those in semiconductors.[10] Consequent nonlinear transport properties constitute the basis for numerous applications, e.g., varistors and boundary layer capacitors.[11,12] In ferroelectric perovskites such as $Sr_xBa_{1-x}TiO_3$ polarization induced compensation of charged grain boundaries and the associated reduction of the Schottky barrier below the Curie temperature gives rise to PTCR behavior.[13]

The properties of grain boundaries in titanate-based oxide ceramics have been extensively studied by macroscopic techniques, such as transport measurements, capacitance, and impedance spectroscopy, etc.[14] These techniques address average properties of grain boundaries and little or no information is obtained about the microscopic structure or details of mesoscopic potential and charge distribution in the vicinity of grain boundaries. The local properties of grain boundaries in $SrTiO_3$ on the atomic level have recently been studied by high resolution transmission electron microscopy, electron-energy-loss spectroscopy, and electron holography,[15–18] and are the subject of intensive theoretical studies.[19,20] Nevertheless, controversy exists regarding the origin of potential at $SrTiO_3$ grain boundaries.[21–24] A direct measure of the local properties of boundaries with well-defined atomic structures would provide considerable insight into this problem. Spatially resolved electrostatic properties of surfaces can be obtained by variants of proximal probe microscopy such as electrostatic force microscopy (EFM) (Refs. 25 and 26) and scanning surface potential microscopy (SSPM).[27,28] In order to address the issue of intrinsic potential at oxide grain boundaries, quantitative analysis of image contrast of a spatially inhomogeneous surface is necessary.

The interpretation of SSPM images on electrically[29,30] and topographically[31] inhomogeneous surfaces has been treated numerically. However, in the case of semiconductor and dielectric surfaces the electrostatic properties of a surface are not characterized solely by intrinsic potential and topography. SSPM images of these surfaces should be interpreted in terms of *effective* surface potential that includes capacitive interactions *per se*, along with contributions from surface and volume bound charges, double layers, and remnant polarization.[32–35] For semiconductor surfaces without Fermi-level pinning, tip-bias induced band bending[36] can lead to a nonlinear surface potential dependence on voltage,[37] further complicating quantification of experimental results. Despite these difficulties, both EFM and SSPM have been applied to semiconductor,[38] organic,[39] and ferroelectric[40,41] surfaces, as well as to defects,[42,43] and photoinduced[44,45] and thermal phenomena[46,47] in these materials. A number of SSPM studies on grain boundary related phenomena have also been reported.[48,49] While these studies have convincingly demonstrated the ability of these techniques to image local potential variation due to point and extended (grain boundary) defects, little or no quantitative information regarding properties was extracted.

The primary limitation of these techniques is that for the general case the relationship between measured force gradient or potential and local properties is influenced by tip geometry, the type of the feedback system, lateral surface inhomogeneity, and surface adsorbates. Obviously, these effects are more pronounced for systems with highly localized lateral variations, e.g., surface, point, and line charges such as charged grain boundaries. Moreover, analytical solutions for the electrostatic problem of a biased tip interacting with charges in an arbitrary configuration (e.g., grain boundary or charged dislocation line) are extremely complicated, rendering quantification of EFM and especially SSPM data virtually impossible.

The present paper presents an approach to quantifying

0163-1829/2000/62(15)/10419(12)/$15.00 PRB 62 ©2000 The American Physical Society

inhomogeneous charge distributions from EFM and SSPM. Using the method of image charges the surface potential distribution in the vicinity of a charged plane with adjacent depletion layers intersecting a surface is determined. A line charge model is used to represent the tip, which treatment incorporates all of the geometric complexity of the problem. From this basis the height dependencies of the force gradient and potential are calculated. While both EFM and SSPM arise from electrostatic interactions, the detection mechanism is fundamentally different; the former is based on the force-gradient induced shift of resonant frequency of mechanically driven cantilever, while the latter employs a nulling scheme to the first harmonic of electrostatic force. The analysis of imaging mechanism in the two cases and comparison to experiment provide a self-consistent result and confirmation of the validity of the calculations. The geometry is chosen to be that of $SrTiO_3$ bicrystal interfaces, but the models can be easily extended to any localized charge distribution on a dielectric surface or within the dielectric.

II. THEORETICAL

Both EFM and SSPM are based on noncontact imaging.[50] The grounded tip first acquires the surface topography using standard intermittent contact atomic force microscopy (AFM). Electrostatic data are collected 50–100 nm above the surface. In EFM, the cantilever is driven mechanically during the noncontact scan. The voltage at the piezoelectric bimorph is $V_{\text{piezo}}=V_{acp}\cos(\omega_p t)$, where the driving frequency ω_p is selected to be equal or close to the resonant frequency of the cantilever ω_0. The oscillating bimorph induces cantilever oscillations at the same frequency and the cantilever deflection is $d=d_0+A(\omega_p)\cos(\omega_p t+\varphi_c)$, where $A(\omega_p)$ is the frequency-dependent oscillation amplitude, φ_c is the phase shift between the driving voltage on the piezobimorph and the cantilever oscillations, and d_0 is the static deflection of the cantilever in the absence of mechanical oscillation. The electrostatic force F between the dc biased conductive tip and the surface results in a change of the cantilever resonant frequency that is proportional to the force gradient[51]

$$\Delta\omega=\frac{\omega_0}{2k}\frac{dF(z)}{dz}, \tag{1}$$

where k is the spring constant. The resonance is maintained by adjusting driving frequency ω_p and the frequency shift $\Delta\omega$ is collected as the EFM image.

In SSPM the cantilever is not driven mechanically; rather, the tip is biased directly by $V_{\text{tip}}=V_{\text{dc}}+V_{\text{ac}}\cos(\omega t)$, where V_{ac} is referred to as the driving voltage. The frequency ω is selected to be equal to the resonant frequency of the cantilever to ensure a strong mechanical response to the electrostatic force between the tip and the surface. The capacitive force, $F_{\text{cap}}(z)$, between the tip and a conductive surface at V_s is

$$F_{\text{cap}}(z)=\frac{1}{2}(V_{\text{tip}}-V_s)^2\frac{\partial C(z)}{\partial z}, \tag{2}$$

where $C(z)$ is the tip-surface capacitance that depends on tip geometry, surface topography and tip-surface separation z. A lock-in technique is used to extract the first harmonic of the force

$$F_{1\omega}^{\text{cap}}(z)=\frac{\partial C(z)}{\partial z}(V_{\text{dc}}-V_s)V_{\text{ac}}\sin(\omega t), \tag{3}$$

which is nullified by adjusting the constant component of the tip bias, V_{dc}. Equation (3) implies that this condition is met when V_{dc} is equal to surface potential and thus, mapping the nulling potential V_{dc} yields a surface potential map.

Quantification of surface properties from the EFM and SSPM data requires the solution of several independent problems, solved here for the case of an interface intersecting a surface. First, these techniques are ultimately sensitive to the force gradient (EFM) or the force (SSPM) between the tip and the surface. The origins of the electrostatic tip-surface interaction and corresponding models are discussed in Sec. II A. Second, the measurements are performed above the grain boundary-surface junction rather than at the grain boundary itself. Therefore, the relationship between the properties of a grain boundary in the bulk and the potential distribution above the surface for ideal surface termination is considered in Sec. II B. The grain boundary contribution to force gradient (EFM data) is considered in Sec. II C. Finally, the influence of a charged grain boundary on the effective potential determined by SSPM and the influence of imaging conditions on SSPM data is discussed in Sec. II D.

A. Tip-surface interaction

For large separations (>10 nm) electrostatic forces between the tip and surface dominate short-range van der Waals forces[52] and for conductive materials are capacitive in nature, i.e., the distance dependence is that of the derivative of tip-surface capacitance. Forces between a dielectric surface and a biased conductive tip are more complicated. Using the analogy between the interaction of a point charge Q and a conductive or a dielectric surface,[53] the electrostatic force can be written as that due to the interaction of charge with the corresponding image charge Q_{im}. For a conductive plane and a dielectric plane the forces are

$$F_{\text{cond}}(z)=-\frac{1}{4\pi\varepsilon_0}\frac{Q^2}{4z^2}, \tag{4a}$$

$$F_{\text{diel}}(z)=-\frac{1}{4\pi\varepsilon_0}\left(\frac{\varepsilon-1}{\varepsilon+1}\right)\frac{Q^2}{4z^2}, \tag{4b}$$

i.e., $Q_{\text{im}}=-Q$ for the metal while $Q_{\text{im}}=-(\varepsilon-1)/(\varepsilon+1)Q$ for the dielectric plane. In both cases, the force is proportional to the square of the charge resulting in a parabolic dependence on the bias voltage. Thus, the interaction force between a dielectric surface and a biased tip can be described in terms of an effective capacitance $C(z,\varepsilon)$, where ε is the dielectric constant of the material. In the limit of high dielectric constant $C(z,\varepsilon)\approx C(z)$. Since the dielectric constant of $SrTiO_3$ is high [$\varepsilon\approx 300$ at 293 K (Ref. 54)], in subsequent analyses the effective capacitance $C(z,\varepsilon)$ is replaced by true capacitance $C(z)$. It should be noted that this assumption is widely used in quantification of EFM data. Even

in this simplified case the tip-surface capacitance and corresponding force depends on the tip geometry, which is rather complicated. A number of geometric models have been used to approximate capacitive tip-surface interactions including a sphere,[55] a hyperboloid,[56–58] a cone,[59] or a cone with spherical apex.[60] An alternative is to use an equivalent image charge such that the corresponding constant potential surface represents the actual tip.[61] Examples are point charge and line charge configurations.[62] Image charge distributions can be also found by numerical methods.[63] The advantage of the image charge approach is that it reduces a complicated boundary-value problem for potential to a much simpler problem of Coulombic charge-charge interaction, while preserving the characteristic features (distance and voltage dependence of the force, tip shape effects) of the original problem.

At small tip-surface separations ($z<R$, where R is tip radius of curvature) where the spherical tip apex provides the major contribution to the force, the bias and distance dependence of the force is best described by sphere or point charge models with a solution of the form

$$F=V^2\frac{\gamma}{z}, \tag{5}$$

where γ is a constant depending on the specific model. For larger tip-surface separations ($z>R$, where R is tip radius of curvature) hyperboloid, cone, or line charge approximations provide the best description. These models predict a logarithmic dependence of capacitive force on tip-surface separation of the general form

$$F=\eta V^2 \ln\left(\frac{D}{z}\right), \tag{6}$$

where η and D are parameters related to the tip geometry.

Within the line charge model the image charge distribution is approximated by a semi-infinite uniformly charged line with line charge density λ. The axially symmetric potential for the line is

$$V(x,z)=\frac{\lambda}{4\pi\varepsilon_0}\ln\left(\frac{d+z+\sqrt{(d+z)^2+x^2}}{d-z+\sqrt{(d+z)^2+x^2}}\right), \tag{7}$$

where d is the distance from the lower end of the line to the surface. It can be shown that

$$d=h\alpha, \tag{8a}$$

where

$$\alpha=\sqrt{1+\tan^2\theta} \tag{8b}$$

and h is the separation between the tip apex and surface and θ is the half-angle of the cone, which is the equipotential surface that represents the tip. The line charge density

$$\lambda=\frac{4\pi\varepsilon_0 V}{\beta}, \tag{9a}$$

where

$$\beta=\ln\left(\frac{1+\cos\theta}{1-\cos\theta}\right) \tag{9b}$$

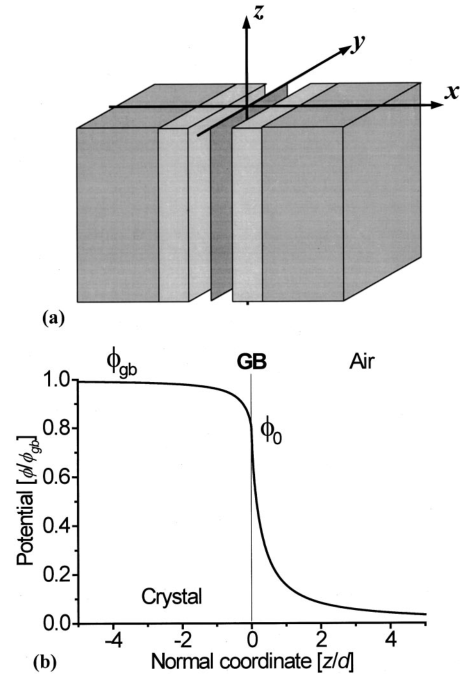

FIG. 1. (a) Simplified charge distribution near the grain boundary and (b) potential near the grain boundary-surface junction for $\varepsilon=4$.

depends on the equipotential surface geometry. The expression for the force is then

$$F_{\text{cap}}=\frac{\lambda^2}{4\pi\varepsilon_0}\ln\left(\frac{(2d+L)^2}{4d(d+L)}\right), \tag{10}$$

where L is the effective tip size. For $d\ll L$ and small angles Eq. (10) reduces to

$$F_{\text{cap}}=\frac{\lambda^2}{4\pi\varepsilon_0}\ln\left(\frac{L}{4h}\right). \tag{11}$$

This relation predicts the logarithmic dependence of capacitive force on tip-surface separation expected from the simple considerations in Eq. (6), but includes the effects of actual tip geometry. Equation (11) is used to calculate the capacitive force and force gradient.

B. Potential at grain boundary-surface junction

In order to quantify the properties of a grain boundary a relationship between the bulk properties and potential above a grain boundary-surface junction is required. Since the potential above the junction is relatively insensitive to the details of charge distribution in the space charge regions, the abrupt junction approximation is used.[64] The grain boundary is characterized by an interface charge density σ and an adjacent space charge layer with width d_{sc}. Charge neutrality requires that $\sigma=-2d_{\text{sc}}\rho_0$, where $\rho_0=e_0N_d$ is the volume charge density, e_0 is the electron charge, and N_d is the ionized donor concentration. The charge distribution in the vicinity of the grain boundary is illustrated in Fig. 1(a). Positive charges at the interface and negative charges in the space-charge region are situated in a medium with dielectric constant ε, i.e., no dielectric constant variation occurs in the vicinity of the boundary. This assumption will be verified

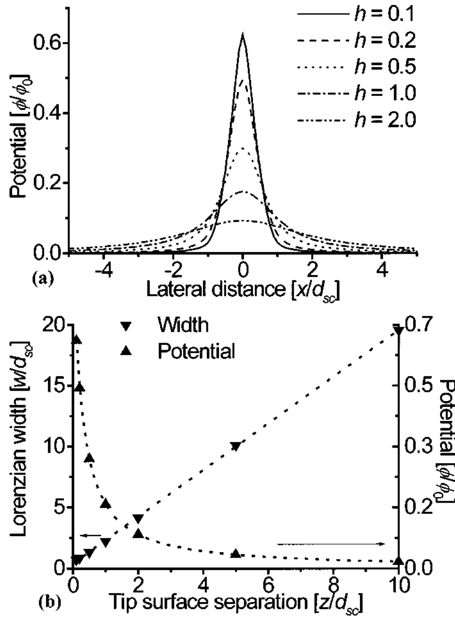

FIG. 2. (a) Potential profiles at different heights above grain boundary-surface junction and (b) grain boundary potential and profile width for different heights.

by the experimental results. The potential distribution in the bulk can be found as a solution of Poisson's equation, which in the abrupt junction approximation yields

$$\varphi(x)=\varphi_{gb}(1-x/d_{sc})^2, \tag{12}$$

for $x<d_{sc}$ and the potential at grain boundary φ_{gb} is

$$\varphi_{gb}=\frac{\rho_0 d_{sc}^2}{2\varepsilon_0\varepsilon}. \tag{13}$$

In order to find the potential above the grain boundary-interface junction the image charge method for a dielectric half-plane is applied:

$$\varphi(\mathbf{r})=\frac{1}{2\pi\varepsilon_0(\varepsilon+1)}\left(\int d\mathbf{r}'\frac{\rho(\mathbf{r}')}{|\mathbf{r}-\mathbf{r}'|}+\int d\mathbf{s}\frac{\sigma(\mathbf{r}'')}{|\mathbf{r}-\mathbf{r}''|}\right), \tag{14}$$

where the volume and surface integrals are taken within space-charge layer and at the interface, respectively. This integral is solved in a closed form, however the resulting expression has a complicated functional form that is not useful for image analysis and is not shown here. Instead the maximal value of potential and the Lorentzian width of the peak are used to describe the potential behavior far from the surface. As expected, the potential achieves a maximum above the grain boundary-surface junction and the calculated potential both within the crystal and above the surface for $\varepsilon=4$ is shown in Fig. 1(b). Within the crystal the potential is almost constant, decreasing only to $\varepsilon/(\varepsilon+1)$ of its bulk value at the boundary. Above the surface the potential decays rapidly. Potential profiles at different heights above the surface are shown in Fig. 2(a). For tip-surface separations $z>0.1d_{sc}$ the potential profile above the junction is well fitted by the Lorentzian function $y=(2A/\pi)w/(4x^2+w^2)$ and the dependence of the width w on separation is shown in Fig. 2(b). The line fit is $w/d_{sc}=0.4+1.9z/d_{sc}$ for $0.1<z/d_{sc}<10$, i.e., within the experimentally accessible region for a typical d_{sc} of order of 100 nm. Therefore, the measured potential profile width as a function of tip-surface separation can be used to determine the size of space-charge layer.

The potential above the surface-interface junction for $x=0$, i.e., the height of potential profile is described by

$$\varphi(z)=\frac{\rho_0}{\pi\varepsilon_0(\varepsilon+1)}\left[(d_{sc}^2-z^2)\arctan\left(\frac{d_{sc}}{z}\right)+d_{sc}z[1+2\ln(z)-\ln(d_{sc}^2+z^2)]\right], \tag{15}$$

which yields $\varphi_0=\varphi(0)=\rho_0 d_{sc}^2/2\varepsilon_0(\varepsilon+1)$ for the potential at the grain boundary-surface junction. The distance dependence of the potential is shown in Fig. 2(b). The relationship between the potential at the grain boundary in the bulk and the potential at the junction has the following form:

$$\varphi_{gb}=\frac{\rho_0 d_{sc}^2}{2\varepsilon_0\varepsilon}=\frac{\varepsilon+1}{\varepsilon}\phi_0. \tag{16}$$

This equation implies that for systems with high dielectric constants the potential at the grain boundary-surface junction directly accessible by scanning probe techniques is almost equal to that at the grain boundary in the bulk. Unfortunately, EFM and SSPM imaging at small tip-surface separations is difficult due to topographic artifacts and imaging instabilities, while for larger tip-surface separations Eq. (15) predicts rapid decay of potential. Nevertheless, provided that the potential is a known function of tip-surface separation, Eq. (15) can be used to extrapolate the lift height-potential dependence to obtain the potential at the junction and Eq. (16) can then be used to determine the grain boundary potential in the bulk. Rewriting Eq. (15) in terms of φ_0 and d_{sc} yields

$$\varphi(z)=\varphi_0\frac{2}{\pi d_{sc}^2}\left[(d_{sc}^2-z^2)\arctan\left(\frac{d_{sc}}{z}\right)+d_{sc}z[1+2\ln(z)-\ln(d_{sc}^2+z^2)]\right]. \tag{17}$$

Noteworthy is that the potential above the grain boundary-surface junction is reduced to a function of only two variables; the potential at the grain boundary-surface junction and the width of the space-charge layer. As expected, Eq. (17) is homogeneous in z/d_{sc} since it is the only length scale in the problem. Fitting the experimental data by Eq. (17) yields φ_0 and d_{sc}. Both EFM and SSPM provide information about the electrostatic forces acting on the tip rather than about the actual potential. Therefore, in the next two sections the forces acting on the tip and their relationship with EFM and SSPM signals are considered.

C. EFM imaging of grain boundary

To quantify the EFM data the grain boundary contribution to the force gradient must be included in the overall interaction. The total force between the biased tip and the surface can be written as

$$F(z)=\frac{dC(z)}{dz}\Delta V^2+\int\frac{\partial\varphi_{gb}}{\partial\mathbf{n}}(\sigma_{tip}+\sigma_{ind})d\mathbf{S}_{tip},\quad(18)$$

where the first term is the capacitive force, $F_{cap}(z)$, discussed in Sec. II A and the second term is a contribution due to the Coulombic interaction of grain boundary charges with the metallic tip, $F_q(z)$. σ_{tip} is the surface charge density of the tip in the absence of a grain boundary, σ_{ind} is the image charge density induced by grain boundary charges, and $\mathbf{n}$ is the normal vector to the tip surface. Assuming that the second term in Eq. (18) is much smaller than the first, i.e., the grain boundary contribution to the EFM signal is small, $\sigma_{ind}\ll\sigma_{tip}$, the charge state of the tip is not influenced by the grain boundary. This justifies the use of the line charge model to describe the Coulombic interaction between the grain boundary and the tip and the second term in Eq. (18) becomes

$$\int\frac{\partial\varphi_{gb}}{\partial\mathbf{n}}\sigma_{tip}d\mathbf{S}_{tip}=\int_d^L\lambda_{tip}\varphi'_{gb}dz\approx\lambda_{tip}\varphi_{gb}(d),\quad(19)$$

since $\varphi_{gb}(z)$ rapidly decays with tip-surface separation. From Eqs. (9a), (11), and (19) the capacitive $F_{cap}(z)$, and Coulombic $F_q(z)$, components of the force are

$$F_{cap}(h)=\frac{4\pi\varepsilon_0V^2}{\beta^2}\ln\left(\frac{L}{4h}\right)\quad(20a)$$

and

$$F_q(h)=\frac{4\pi\varepsilon_0V}{\beta}\varphi_{gb}(\alpha h).\quad(20b)$$

The force gradients proportional to the frequency shift measured in EFM are

$$\frac{dF_{cap}}{dz}=\frac{4\pi\varepsilon_0V^2}{\beta^2}\frac{1}{h},\quad(21a)$$

$$\frac{dF_q}{dz}=\frac{4\pi\varepsilon_0V\alpha}{\beta}\varphi'_{gb}(\alpha h).\quad(21b)$$

The spring constant that relates the experimentally determined frequency shift and force gradient [Eq. (1)] is usually unknown and depends strongly on cantilever properties. However, the ratio of frequency shift at the grain boundary to that of the surface is independent of cantilever properties and is equal to

$$\frac{F'_q}{F'_{cap}}=\frac{\alpha\beta}{V}h\varphi'_{gb}(\alpha h).\quad(22)$$

From Eq. (17) the gradient of grain boundary potential can be found as

$$\varphi'_{gb}(z)=\varphi_0\frac{2}{\pi d_{sc}^2}\left[-4z\arctan\left(\frac{d_{sc}}{z}\right)+2d_{sc}[2+2\ln(z)-\ln(d_{sc}^2+z^2)]\right].\quad(23)$$

By fitting the measured ratio with the function

$$F_{ratio}=\frac{F'_q}{F'_{cap}}=\frac{A}{\pi d_{sc}^2}z\left[4\alpha z\arctan\left(\frac{d_{sc}}{\alpha z}\right)-2d_{sc}[2+2\ln(\alpha z)-\ln(d_{sc}^2+\alpha^2z^2)]\right],\quad(24)$$

where A and d_{sc} are now fitting parameters and α is given in Eq. (8b), both the space-charge layer width d_{sc} and potential at the grain boundary-surface junction φ_0 can be extracted as

$$\varphi_0=\frac{AV}{\sqrt{1+\tan^2\theta}}\left\{\ln\left(\frac{1+\cos\theta}{1-\cos\theta}\right)\right\}^{-1},\quad(25)$$

where θ is tip half-angle. The width of the EFM profile provides an independent measurement of d_{sc}.

D. SSPM imaging of grain boundaries

Quantification of SSPM contrast is treated similar to that for EFM contrast, using the line charge description of the tip. The electrostatic force between the tip and the surface is described by Eqs. (11) and (18) and the first harmonic of capacitive force is

$$F_{1\omega}^{cap}=\frac{4\pi\varepsilon_0V_{ac}(V_{dc}-V_s)}{\beta^2}\ln\left(\frac{L}{4h}\right),\quad(26)$$

where V_s is the effective surface potential originating from intrinsic surface states or adsorbates. The first harmonic of Coulombic force is

$$F_{1\omega}^{q}=4\pi\varepsilon_0V_{ac}\left\{\ln\left(\frac{1+\cos\theta}{1-\cos\theta}\right)\right\}^{-1}\varphi_{gb}(h\sqrt{1+\tan^2\theta}).\quad(27)$$

During the measurement a feedback loop nullifies the first harmonic of the force; however, under typical operating conditions it is reduced to some small, but finite value $\tilde{\delta}$ dependent on circuit parameters.[31] Thus, during SSPM imaging the observed signal satisfies the condition

$$F_{1\omega}^{\Sigma}=F_{1\omega}^{q}+F_{1\omega}^{cap}=\tilde{\delta}.\quad(28)$$

Substituting Eqs. (26) and (27) in Eq. (28) the first harmonic of the force is

$$\frac{V_{ac}(V_{dc}-V_s)}{\beta}\ln\left(\frac{L}{4h}\right)+V_{ac}\varphi_{gb}(\alpha h)=\delta,\quad(29)$$

where

$$\delta=4\pi\varepsilon_0\ln\left(\frac{1+\cos\theta}{1-\cos\theta}\right)\tilde{\delta}\quad(30)$$

depends on the geometric properties of the tip but not on the tip-surface separation. The cantilever contribution to the total electrostatic force can be assumed to be distance independent, since the effective cantilever-surface separation ($\sim$10–15 μm) is much larger than the tip-surface separation ($<$1 μm) and leads to a higher value of the parameter L in Eq. (29). From Eq. (29) the nulling potential measured in SSPM is

$$V_{\rm dc}=V_{\rm s}-\beta\frac{\varphi_{\rm gb}(\alpha h)}{\ln(L/4h)}+\frac{\delta}{V_{\rm ac}\ln(L/4h)}. \quad (31)$$

The average image potential far from the boundary is

$$V_{\rm dc}=V_{\rm s}+\frac{\delta}{V_{\rm ac}\ln(L/4h)}. \quad (32)$$

In ideal SSPM imaging the nulling voltage is equal to surface potential and does not depend on tip-surface capacitance and driving voltage. This corresponds to $\delta=0$ in Eq. (31), i.e., ideal feedback. For a realistic system, however, Eq. (31) predicts a nulling voltage (SSPM signal) dependence on tip-surface separation and driving amplitude. The deviation of feedback from ideality and the tip geometry are thus described by a single parameter δ. The potential contrast due to the grain boundary is then the difference of $V_{\rm dc}$ above the boundary and far from the boundary

$$\Delta V_{\rm dc}=\beta\frac{\varphi_{\rm gb}(\alpha h)}{\ln(L/4h)}. \quad (33)$$

Provided that experimental SSPM contrast follows Eq. (32), i.e., feedback error is described by single parameter δ and grain boundary potential is independent of driving voltage as suggested by Eq. (33), fitting the experimentally determined distance dependence of potential amplitude at the grain boundary by the function

$$\Psi(z)=\frac{\beta\varphi_0}{c-\ln(z)}\frac{2}{\pi d_{\rm sc}^2}\left[(d_{\rm sc}^2-\alpha^2z^2)\arctan\left(\frac{d_{\rm sc}}{\alpha z}\right)+\alpha d_{\rm sc}z[1+2\ln(\alpha z)-\ln(d_{\rm sc}^2+\alpha^2z^2)]\right], \quad (34)$$

where c, $d_{\rm sc}$, and φ_0 are fitting parameters and α and β parameters defined by Eqs. (8b) and (9b), can be used to extract the space-charge width $d_{\rm sc}$, and the potential at the grain boundary-surface junction φ_0. The parameter $c=\ln(L/4)$ is related to the tip and cantilever geometry.

Thus, EFM and SSPM provide two independent methods to determine the grain boundary potential and depletion width; one based on force gradient measurements, one based on nulling force measurements. Analysis of both EFM and SSPM data will provide quantitative information about the $SrTiO_3$ grain boundaries.

III. EXPERIMENTAL PROCEDURES

In order to relate the grain boundary properties to atomic configuration, an interface with a known structure was used. Nb-doped $\Sigma 5$ $SrTiO_3$ bicrystals (0.5 wt %) were produced by diffusion bonding. Numerous high resolution transmission electron microscopy studies on similar bicrystals have shown that the interfaces are atomically abrupt, with no impurity segregation.[65,66] Scanning probe studies indicate the presence of pores at the interface. A $10\times10\times0.5\text{-mm}^3$ crystal, dark blue due to the donor doping, is sectioned such that the grain boundary is perpendicular to the (100) surface. The grain boundary can be easily detected by means of transmission optical microscopy as a dark blue (almost black) line on the lighter background perpendicular to the edge of the crystal. Topographic features were used as markers to determine the position of grain boundaries in the EFM and SSPM measurements; very often a wedgelike divot is associated with the grain boundary-crystal edge junction. Prior to imaging the crystal was repeatedly washed with ethanol, acetone, and distilled water.

The AFM, EFM, and SSPM measurements were performed on a commercial instrument (Digital Instruments Dimension 3000 NS-III) with metal coated tips ($l\approx225\ \mu$m, resonant frequency $\sim$70 kHz). SSPM measurements were performed from 0 to 1.5 μm above the surface; EFM measurements were performed from 20 to 200 nm above the surface. The scan rate varied from 0.2 to 0.5 Hz. The driving voltage dependence of surface potential observed by SSPM saturates at driving voltage $\sim$1–2 V for the lift heights of interest; therefore, $V_{\rm ac}$ was chosen to be $>$5 V. To reduce the effect of drift the images were acquired with the grain boundary oriented along the slow scan axis. Topographic and EFM images were processed by line flattening.[67] SSPM images were processed only by a constant background subtraction. Force gradient and potential profiles were obtained by averaging the flattened EFM and unprocessed SSPM images along the slow scan axis. A generic feature of SSPM is fewer imaging artifacts due to topography (Fig. 3). The use of a low dc bias voltages contributes to higher image stability. Also, detection in SSPM implies a much smaller tip oscillation amplitude than that in topographic or EFM imaging. From a direct comparison of the signal from the photodiode in the main scan line and noncontact scan line the characteristic oscillation amplitude during potential detection is $<$1 nm depending on feedback circuit parameters.[68] Thus, for flat surfaces imaging is possible at very small tip-surface separation.

IV. RESULTS

The experimental force and force gradient measurements of the grain boundary in Nb-doped $\Sigma 5$ $SrTiO_3$ bicrystals are shown in the following order. In Sec. IV A surface topography, surface potential and force gradient in the vicinity of the grain boundary are presented. The bias and lift height dependencies of force gradient (EFM) images are analyzed in Sec. IV B; the influence of feedback parameters and the lift height dependence on the SSPM images is discussed in Sec. IV C.

A. AFM, EFM, and SSPM imaging

The surface topography, surface potential, and force gradients of the grain boundary-surface intersection are compared in Fig. 3. The surface is extremely flat with rms roughness $<$1 nm and a number of spots due to contaminates. Pores with diameters of $\sim$100–200 nm are distributed nonuniformly along the interface. This observation suggests that the pores exist in the bulk as well and contribute to the optical contrast of the grain boundary. Similar observations of pores at $SrTiO_3$ bicrystal interfaces are reported by other groups.[69] The surface potential measured 50 nm above the surface exhibits a sharp protrusion associated with the grain boundary, Fig. 3(b). The halfwidth of the broad potential feature is $\sim$1.5 μm. Superimposed on this contrast is a much narrower and larger amplitude feature of halfwidth $\sim$200 nm localized at the grain boundary. The force gradient images

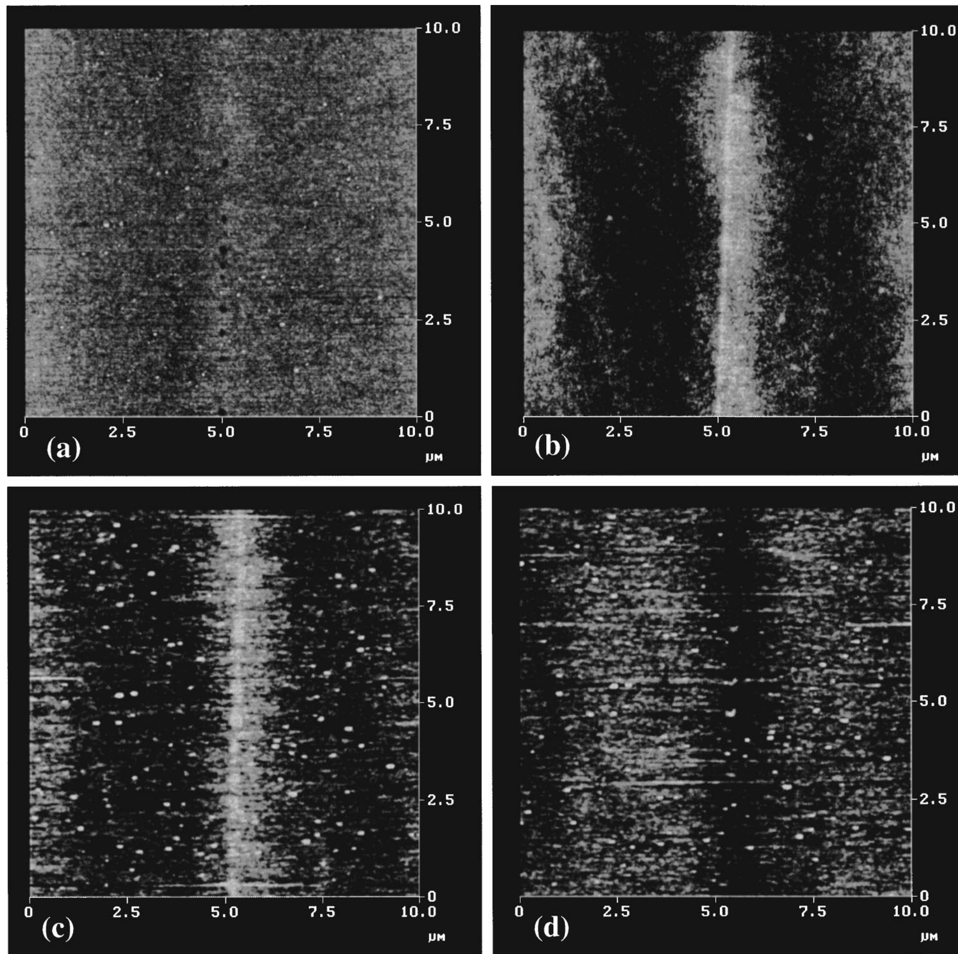

FIG. 3. (a) Topography of Nb-doped 36.8° $SrTiO_3$ bicrystal in the vicinity of grain boundary, (b) SSPM image of the same region, and (c) EFM (force gradient) images at tip bias $V_{tip}=5$ V and $V_{tip}=-5$ V. Range is (a) 5 nm, (b) 20 mV, and (c),(d) 2 Hz.

acquired with +5 and −5 V tip bias are shown in Figs. 3(c) and 3(d). The grain boundary is again associated with a feature of halfwidth ~1.5 μm. The contrast in the force gradient image reverses with tip polarity, indicative of a dominant Coulombic contribution to the interaction.

B. Bias and distance dependence of EFM image

To quantify the bias dependence of capacitive force the average frequency shift due to the surface, defined as the image average of the unprocessed image, is analyzed by Eqs. (1) and (21a). The difference between the maximum frequency shift at the grain boundary and the frequency shift far from the grain boundary is referred to as the grain boundary frequency shift. In order to improve the estimates for large separations, force gradient profiles were fitted by a Lorentzian function. The bias dependence of the average frequency shift and grain boundary frequency shift are compared in Fig. 4. As expected, the average frequency shift is a parabolic function of bias voltage, $\Delta\omega_{im}=\Delta\omega_0+a(V-V_s)^2$, where $\Delta\omega_{im}$ is the total frequency shift, $\Delta\omega_0$ is the frequency offset, V_s is the potential offset, and a is a proportionality constant (Table I). The potential offset V_s is related to the existence of a double layer due to intrinsic surface states or adsorption as well as to the work function difference between the tip and the surface. The frequency offset $\Delta\omega 0$

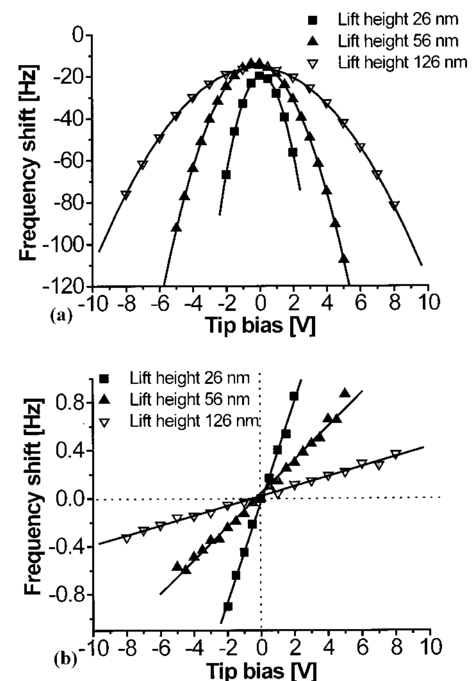

FIG. 4. (a) Total frequency shift (image average) and (b) frequency shift due to grain boundary as a function of tip bias.

TABLE I. EFM bias-dependence fitting parameters.

Lift height (nm)	$\Delta\omega_0$ (Hz)	V_s (mV)	a (Hz/V^2)	Slope (Hz/V)
26	-19.6 ± 0.2	117 ± 5	-10.4 ± 0.1	0.42 ± 0.01
56	-13.9 ± 0.1	-216 ± 3	-3.44 ± 0.01	0.140 ± 0.003
126	-15.7 ± 0.1	-188 ± 5	-0.986 ± 0.002	0.041 ± 0.001

≈ 10 Hz is due to drift in the oscillating characteristics of the cantilever after calibration. The dependence of the grain boundary frequency shift on bias voltage is shown in Fig. 4(b). This dependence is linear and intersects the origin. These results indicate that the average force interaction originates from a capacitive tip-surface interaction, thus the quadratic bias dependence. The grain boundary component to the EFM contrast is linear in tip bias and therefore can be attributed to Coulombic interactions of charges at the grain boundary with the biased tip [compare Eqs. (21a) and (21b)]. The magnitude of the former effect is much larger than that of the latter, in agreement with the assumptions.

The distance dependencies of the average frequency shift and the grain boundary frequency shift are shown in Fig. 5(a) for tip biases of 5 and -5 V. For small tip-surface separations the dependence in log-log coordinates is almost linear with a slope close to unity, in agreement with Eq. (21a). In order to take into the account frequency offset $\Delta\omega_0$, the following fitting function is used:

$$\Delta\omega_{\mathrm{im}}=b+\frac{c}{z}, \tag{35}$$

where $\Delta\omega_{\mathrm{im}}$ is total frequency shift; b and c are fitting parameters. For tip biases of 5 and -5 V, $b=7.8\pm1.7$ Hz, $c=6200\pm115$ nm/s and $b=3.2\pm3.5$ Hz, $c=6431\pm295$ nm/s, respectively. The frequency shift can be found from Eqs. (1) and (21a) as

$$\Delta\omega_{\mathrm{im}}=\frac{\omega_0}{2k}\frac{4\pi\varepsilon_0 V^2}{\beta^2}\frac{1}{h}. \tag{36}$$

Substituting the resonant frequency of the cantilever $\omega_0=76.6$ kHz, a typical spring constant for the tip $k=1-5$ N/m and a typical tip half-angle $\theta\approx17°$, the frequency shift according to Eq. (36) yields coefficient c equal to 6400–1290 nm/s, which is in excellent agreement with our experimental results. From this the cantilever spring constant for the probe used is 1 N/m.

The lift height dependence for the grain boundary frequency shift shown in Fig. 5(b) was also quantified. The force gradient maxima were fitted by Eqs. (23) and (25) yielding $A=152\pm3$, $d=229\pm15$ nm for $V=5$ V and $A=142\pm4$, $d=217\pm32$ nm for $V=-5$ V.

From Eqs. (1) and (21b) the frequency shift for the grain boundary is

$$\Delta\omega_{\mathrm{gb}}=\frac{\omega_0}{2k}\frac{4\pi\varepsilon_0 V\alpha}{\beta}\varphi'_{\mathrm{gb}}(\alpha h). \tag{37}$$

Using the same tip parameters, these results yield the potential at the grain boundary-surface junction as 30–140 mV. Using the spring constant derived from the total frequency shift-distance analysis, the potential at the grain boundary-surface junction is $\sim$30 mV.

Finally, the cantilever-dependent constant in Eq. (1) can be eliminated by taking the *ratio* of experimentally observed grain boundary frequency shift and total frequency shift. The ratio and the fit by Eq. (24) are shown in Fig. 6. Using tip parameters $\theta\approx17°$, $\alpha\approx1.04$, $\beta\approx4.1$, the depletion width is 240 nm and the potential at grain boundary-surface junction is 29 mV.

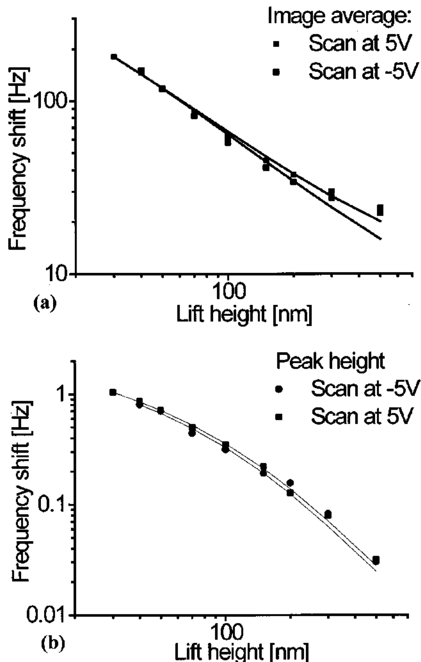

FIG. 5. (a) Fitting the total frequency shift (image average) and (b) frequency shift due to grain boundary as a function of tip-surface separation for tip biases 5 and -5 V.

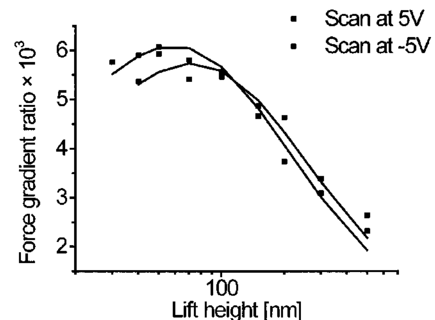

FIG. 6. Fitting the ratio of frequency shift due to grain boundary to total frequency shift as a function of tip-surface separation for tip biases 5 and -5 V.

TABLE II. Driving voltage dependence of SSPM image average.

Lift height (nm)	V_s (mV)	$B=\delta \ln(L/4h)$
10	-89 ± 2	85 ± 1
30	-147 ± 3	103 ± 2
50	-117 ± 3	135 ± 3
0	323 ± 12	122 ± 3

C. Driving amplitude and distance dependence of SSPM image

Quantification of SSPM data is done similarly to that of EFM data, i.e., average image potential and potential difference between the grain boundary and the rest of the image were determined. Both driving voltage and tip-surface separation dependencies were measured. According to Eq. (3), surface potential measured by SSPM should be independent of bias voltage. In practice, however, the nonideality of the feedback loop results in $1/V_{ac}$ dependence on driving amplitude as shown in Eq. (31). Thus, the average image potential V_{av} is fit by $V_{av}=V_s+B/V_{ac}$, where V_s is surface potential and B is a fitting parameter [compare Eq. (31)]. The results are summarized in Table II and illustrated in Fig. 7(a). Noteworthy is that the measured potential amplitude due to the grain boundary ΔV_{gb} is virtually V_{ac} independent above 2 V as seen in Fig. 7(b). At low driving voltages there is considerable noise and possibly a small increase in potential. However, this effect does not exceed ~2–4 mV, while the dependence of the average image potential [see Fig. 8(a)] indicates a strong driving voltage dependence. This observation implies that grain boundary potential amplitudes obtained by SSPM are relatively insensitive to imaging conditions and Eq. (34) can be used to describe potential-distance relation, i.e., the third term in Eq. (31) is indeed irrelevant to observed grain boundary potential amplitudes. This demonstrates that system parameters that strongly influence the absolute value of measured surface potential do not alter measured potential variations.

The distance dependence for different driving voltages is shown in Fig. 8(a). These results are in a qualitative agreement with Eq. (32), i.e., V_{dc} is higher for small driving voltages. Of course, the range of the data exceeds that of the assumptions; however, the results seem to demonstrate a driving voltage dependence of the average surface potential. In contrast, the distance dependence of grain boundary potential is independent of driving voltage as shown in Fig. 8(b). The noise is significantly higher for low driving voltages. The grain boundary potential-distance dependence fitted by Eq. (34) is shown in Fig. 9. Depletion width and potential at the grain boundary-surface junction determined from these data are 147 ± 21 nm and 28 ± 4 mV, respectively. Note the excellent agreement with the properties obtained from the quantification of EFM measurements despite the difference in imaging mechanism and analysis. From the fit we also estimate that the parameter $c\approx8.8\pm0.7$ is close to the ideal value $c\approx8$ for the real tips. The larger value of c in the measurement is consistent with a contribution of cantilever to the electrostatic force.

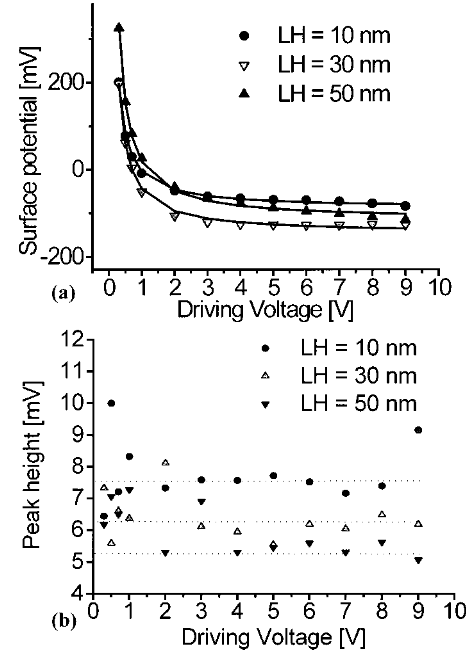

FIG. 7. (a) Dependence of characteristic surface potentials on driving voltage for different lift heights (only three curves are shown) and (b) average potential barrier height as a function of driving voltage for different lift heights.

V. DISCUSSION

The origins of grain boundary potential can be addressed within the context of these results by considering the magnitude and bias dependence of the measured potential as related to the structure of the grain boundary. When viewed in cross section, looking at the (100) plane, the atomic structure

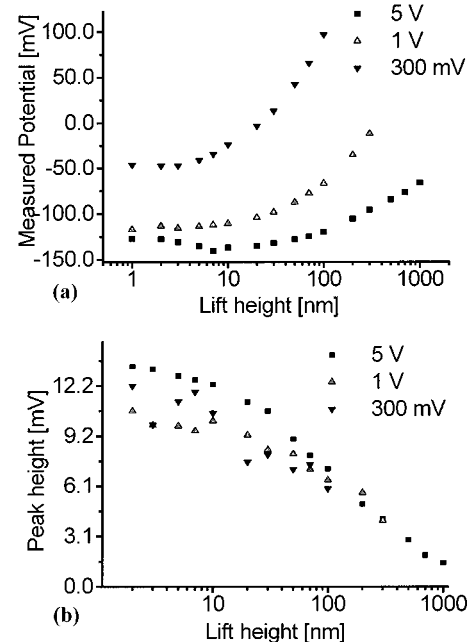

FIG. 8. (a) Dependence of average surface potentials on lift height in the interleave mode for different driving voltages and (b) average potential barrier height as a function of lift height for different driving voltages.

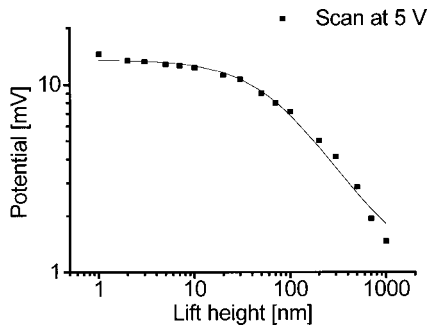

FIG. 9. Fit of potential barrier height determined by SSPM as a function of lift height.

of the Σ5 boundary consists of two alternating pentagonal oxygen structural units containing two Sr columns and two Ti columns, respectively. In both units the cation positions are half occupied, forming a grain boundary reconstruction.[65,70,71] If the requisite number of oxygen atoms reside at the grain boundary, it is stoichiometric and neutral in terms of formal charge. In this case the boundary potential can arise from local dielectric constant variation or local redistribution of charge density. If the grain boundary is oxygen deficient, then the Ti will be partially reduced and the interface carries formal charge compensated by free carriers in an adjacent depletion region.

Contrast reversal in the force gradient with bias indicates the presence of a nonuniform charge distribution in the vicinity of the grain boundary, rather than a variation of effective dielectric constant. The latter possibility would alter the ''apparent'' grain boundary potential but not reverse the sign. A local dielectric constant variation would also produce a deviation from linearity in the bias dependence, which is not observed in Fig. 4(b). Therefore, any local variation in dielectric constant makes a negligible contribution to the measured boundary potential. Further confirmation of the presence of charge comes from the fact that tip parameters extracted from these analyses are in excellent agreement with each other and with the properties of actual tip.

Quantification of both the EFM and SSPM results lead to a depletion width of $d_{sc} \approx 200\,\mathrm{nm}$ and a potential of $\phi_{gb} \approx 30\,\mathrm{mV}$ for this grain boundary. From Eq. (13) the volume charge density is $4.0\times 10^3\,\mathrm{C/m^3}$ and interface charge density is $1.6\times 10^{-3}\,\mathrm{C/m^2}$, or carrier concentrations are $2.5\times 10^{16}\,\mathrm{cm^{-3}}$ and $5.0\times 10^{11}\,\mathrm{cm^{-2}}$, respectively. If the grain boundary is considered to be a single plane, this charge is equivalent to one oxygen vacancy every 10 000, which is an extremely small number. In certain well-defined grain boundaries with different crystallographic structure, interface potentials on the order of 300–400 mV have been determined by SSPM.[72] Even at these potentials the implied interface defect concentration is so low as to be at the detection limit of current imaging tools. However, recent localized energy loss spectroscopy as well as calculations provide evidence of reduced Ti in the boundary core structure.[20,73]

Grain boundary properties have been measured on $SrTiO_3$ bicrystals by bulk techniques, for example electron holography, high temperature transport, or impedance spectroscopy.[22,66] In certain cases where comparisons were made on very similar crystals, EFM/SSPM yields values of interface potential close to those from ionic transport measurements, i.e., the grain boundary potential at the surface is the same as that in bulk.[72] In the present case, however, the grain boundary potential at the surface is substantially lower than that expected in the bulk. The self-consistency of the results presented here provide strong support for the validity of the EFM and SSPM measurements. Thus, the grain boundary potential at the surface in this case may actually be lower than in the bulk or the crystal may differ from those used in the studies that determined the ''expected'' value. A lower potential at the surface could result from damage or surface adsorption. A small variation in thermal history would alter the bulk grain boundary properties.

One of the significant advantages of scanning probes is that the potential distribution is imaged in real space and fine details can be examined. In this regard the origins of the abnormal width of the grain boundary potential feature remains unresolved. The space-charge depth was quantified from analysis of the distance dependence of amplitudes of potential contrast, thus eliminating the tip broadening effects. However, the width of the observed grain boundary contrast (~1.5 μm) is much larger than the depletion width obtained from distance dependencies (~200 nm) and, as suggested by finite element modeling, cannot be accounted for by tip shape effects.[30,74] Also note that the potential distribution is nonuniform within the broad feature (Fig. 3), exhibiting a narrow peak with the ''correct'' shape superimposed on a wide asymmetric region. The origins of the asymmetric feature may include surface mobile charges,[32] composition gradients, or stress-induced dislocation redistribution, perhaps exacerbated by surface reactivity. Indeed, adsorption of charged impurities in the vicinity of the grain boundary would result in a decrease of absolute potential amplitude and an increase of the apparent size of the grain boundary. This explanation also accounts for the unusual shape of the potential and force-gradient feature at the grain boundary. It is also possible that the mesoscopic defects (pores) at the interface and related stresses or trapped charges cause a potential gradient that is superimposed on the intrinsic grain boundary response. A similar interpretation was given by Hsu[69] to explain near field optical measurements.

Finally, the self-consistency of the properties from EFM and SSPM calculations and the accuracy to which the tip parameters extracted from the model reflect the actual tip verify the validity of the theoretical model. The V_{ac} dependence of SSPM contrast verifies that assumptions made for the analysis of distance dependence of effective grain boundary potential are also correct. One reason that the model works so well is that the equipotential description of the tip allows for the actual tip shape. For different tip shapes, the voltage and distance dependencies will still yield grain boundary potentials and widths. The tip shape parameters extracted from the data would then reflect the new tip shape. The accuracy does not depend on whether the tip adopts an accommodating shape such as a cone or sphere. The solutions for sample inhomogeneity presented here pertain to a plane of charge intersecting a surface, but can be easily extended to any localized charge distribution in a dielectric.

VI. CONCLUSION

An analytical approach for the quantification of EFM and SSPM data for the systems with potential inhomogeneities

has been developed in order to determine the interface potential in a donor-doped Σ5 $SrTiO_3$ grain boundary. The voltage dependencies of the electrostatic force gradient and surface potential verified the solutions and the distance dependencies of force gradient and potential were used to determine the potential at the grain boundary-surface junction and the depletion width. Both measurements yielded virtually the same properties despite the different imaging mechanisms. The interface potential is shown to result from local charge rather than from the local variation in dielectric constant. The amount of charge implied by and interface potential of 30 mV would render detection of associated defects impossible, but it should be noted that these results may be mediated by surface adsorption and therefore represent a lower limit of a true grain boundary potential.

ACKNOWLEDGMENTS

We acknowledge the support from MRSEC Grant No. NSF DMR96-32596. The authors are grateful to G. Duscher and S. Pennycook for bicrystal samples and D. L. Gorbachev for the development of image analysis software.

*Corresponding author: bonnell@sol1.lrsm.upenn.edu

[1] L. L. Hench and J. K. West, *Principles of Electronic Ceramics* (Wiley, New York, 1990).
[2] M. E. Lines and A. M. Glass, *Principles and Applications of Ferroelectric and Related Materials* (Oxford University Press, New York, 1977).
[3] G. H. Haertling, J. Am. Ceram. Soc. **82**, 797 (1999).
[4] J. G. Bednorz and K. A. Muller, Z. Phys. B: Condens. Matter **64**, 189 (1986).
[5] C. N. R. Rao, R. Manesh, A. K. Raychaudhuri, and R. Mahendiran, J. Phys. Chem. Solids **59**, 487 (1998).
[6] L. L. Balcells, J. Fontcuberta, B. Martinez, and X. Obradors, J. Phys.: Condens. Matter **10**, 1883 (1998).
[7] B. Huybrechts, K. Ishizaki, and M. Takata, J. Mater. Sci. **30**, 2463 (1995).
[8] A. Amin and R. E. Newnham, Key Eng. Mater. **66&67**, 339 (1992).
[9] S. B. Desu, Key Eng. Mater. **66&67**, 375 (1992).
[10] S. M. Sze, *Physics of Semiconductor Devices* (Wiley, New York, 1981).
[11] Y. Xu, *Ferroelectric Materials and Their Applications* (North-Holland, Amsterdam, 1991).
[12] S. B. Desu and D. A. Payne, J. Am. Ceram. Soc. **73**, 3416 (1990).
[13] W. Heywang, J. Mater. Sci. **6**, 1214 (1971).
[14] N. S. Hari, P. Padmini, and T. R. N. Kutty, J. Mater. Sci.: Mater. Electron. **8**, 15 (1997).
[15] M. M. McGibbon, N. D. Browning, A. J. McGibbon, and S. J. Pennycook, Philos. Mag. A **73**, 625 (1996).
[16] N. D. Browning, H. O. Moltaji, and J. P. Buban, Phys. Rev. B **58**, 8289 (1998).
[17] F. Ernst, O. Kienzle, and M. Ruhle, J. Eur. Ceram. Soc. **19**, 665 (1999).
[18] N. D. Browning and S. J. Pennycook, J. Phys. D **29**, 1779 (1996).
[19] G. Duscher, J. P. Buban, N. D. Browning, M. F. Chisholm, and S. J. Pennycook (unpublished).
[20] S.-D. Mo, W. Y. Ching, M. F. Chisholm, and G. Duscher, Phys. Rev. B **60**, 2416 (1999).
[21] V. Ravikumar, R. P. Rodrigues, and V. P. Dravid, Phys. Rev. Lett. **75**, 4063 (1995).
[22] Z. Mao, R. E. Dunin-Borkowski, G. B. Boothroyd, and K. M. Knowles, J. Am. Ceram. Soc. **81**, 2917 (1998).
[23] V. Ravikumar, R. P. Rodrigues, and V. P. Dravid, J. Phys. D **29**, 1799 (1996).
[24] Y.-M. Chiang and J. A. S. Ikeda, Ceram. Trans. **41**, 3 (1994).
[25] R. Wiesendanger, *Scanning Probe Microscopy and Spectroscopy—Methods and Applications* (Cambridge University Press, Cambridge, UK, 1994).
[26] *Electric Force Microscopy (EFM)*, Digital Instruments Support Note SN230, 1996.
[27] J. M. R. Weaver and D. W. Abraham, J. Vac. Sci. Technol. B **9**, 1559 (1991).
[28] M. Nonnenmacher, M. P. O'Boyle, and H. K. Wickramasinghe, Appl. Phys. Lett. **58**, 2921 (1991).
[29] A. K. Henning and T. Hochwitz, Mater. Sci. Eng., B **42**, 88 (1996).
[30] H. O. Jacobs, P. Leuchtmann, O. J. Homan, and A. Stemmer, J. Appl. Phys. **84**, 1168 (1998).
[31] S. Cohen and A. Efimov (unpublished).
[32] K. Domansky, Y. Leng, C. C. Williams, J. Janata, and D. Petelenz, Appl. Phys. Lett. **63**, 1513 (1993).
[33] S. Cunningham, I. A. Larkin, and J. H. Davies, Appl. Phys. Lett. **73**, 123 (1998).
[34] K. Franke, H. Huelz, and M. Weihnacht, Surf. Sci. **41**, 178 (1998).
[35] S. V. Kalinin and D. A. Bonnell, J. Appl. Phys. (to be published).
[36] C. Donolato, Phys. Rev. B **54**, 1478 (1996).
[37] Y. Leng, C. C. Williams, L. C. Su, and G. B. Stringfellow, Appl. Phys. Lett. **66**, 1264 (1995).
[38] M. Tanimoto and O. Vatel, J. Vac. Sci. Technol. B **14**, 1547 (1996).
[39] M. Fujihira, Annu. Rev. Mater. Sci. **29**, 353 (1999).
[40] X. Q. Chen, H. Yamada, T. Horiuchi, K. Matsushige, S. Watanabe, M. Kawai, and P. S. Weiss, J. Vac. Sci. Technol. B **17**, 1930 (1999).
[41] T. Tybell, C. H. Ahn, and J.-M. Triscone, Appl. Phys. Lett. **75**, 856 (1999).
[42] P. M. Bridger, Z. Z. Bandic, E. C. Piquette, and T. C. McGill, Appl. Phys. Lett. **74**, 3522 (1999).
[43] Q. Xu and J. W. P. Hsu, J. Appl. Phys. **85**, 2465 (1999).
[44] A. Chavez-Pirson, O. Vatel, M. Tanimoto, H. Ando, H. Iwamura, and H. Kanbe, Appl. Phys. Lett. **67**, 3069 (1995).
[45] T. Meoded, R. Shikler, N. Fried, and Y. Rosenwaks, Appl. Phys. Lett. **75**, 2435 (1999).
[46] S. V. Kalinin and D. A. Bonnell, Z. Metallkd. **90**, 983 (1999).
[47] E. Z. Luo, Z. Xie, J. B. Xu, I. H. Wilson, and L. H. Zhao, Phys. Rev. B **61**, 203 (2000).
[48] B. D. Huey, D. Lisjak, and D. A. Bonnell, J. Am. Ceram. Soc. **82**, 1941 (1999).
[49] Q. Xu and J. W. P. Hsu, Phys. Rev. Lett. **82**, 612 (1999).
[50] Q. Zhong, D. Innis, K. Kjoller, and V. Elings, Surf. Sci. **290**, 1688 (1993).
[51] D. Sarid, *Scanning Force Microscopy* (Oxford University Press, New York, 1991).
[52] M. Saint Jean, S. Hudlet, C. Guthmann, and J. Berger, J. Appl. Phys. **86**, 5245 (1999).

[53] J. D. Jackson, *Classical Electrodynamics* (Wiley, New York, 1998).
[54] *Landolt-Börnstein, New Series*, Group III: Crystals and Solid State Physics, edited by K.-H. Hellwege and A. M. Hellwege (Springer, New York, 1981), Vol. 16a.
[55] B. D. Terris, J. E. Stern, D. Rugar, and H. J. Mamin, Phys. Rev. Lett. **63**, 2669 (1989).
[56] N. M. Miskovsky, P. H. Cutler, and T. E. Feuchtwang, Int. J. Infrared Millim. Waves **2**, 739 (1981).
[57] L.-H. Pan, T. E. Sullivan, V. J. Peridier, P. H. Cutler, and N. M. Miskovsky, Appl. Phys. Lett. **65**, 2151 (1994).
[58] J. He, P. H. Cutler, N. M. Miskovsky, and T. E. Feuchtwang, Surf. Sci. **246**, 348 (1991).
[59] H. Yokoyama, T. Inoue, and J. Itoh, Appl. Phys. Lett. **65**, 3143 (1994).
[60] S. Hudlet, M. SaintJean, C. Guthmann, and J. Berger, Eur. Phys. J. B **2**, 5 (1998).
[61] G. Mesa, E. Dobado-Fuentes, and J. J. Saenz, J. Appl. Phys. **79**, 39 (1996).
[62] H. W. Hao, A. M. Baro, and J. J. Saenz, J. Vac. Sci. Technol. B **9**, 1323 (1991).
[63] S. Belaidi, P. Girard, and G. Leveque, J. Appl. Phys. **81**, 1023 (1997).
[64] W. Monch, *Semiconductor Surfaces and Interfaces*, Springer Series in Surface Sciences Vol. 26 (Springer, New York, 1993).
[65] N. D. Browning, J. P. Buban, H. O. Moltaji, S. J. Pennycook, G. Duscher, K. D. Johnson, R. P. Rodrigues, and V. P. Dravid, Appl. Phys. Lett. **74**, 2638 (1999).
[66] K. D. Johnson and V. P. Dravid, Appl. Phys. Lett. **74**, 621 (1999).
[67] *Command Reference Manual* (Digital Instruments, Santa Barbara, 1997).
[68] H. O. Jacobs, H. F. Knapp, and A. Stemmer, Rev. Sci. Instrum. **70**, 1756 (1999).
[69] E. B. McDaniel, S. C. McClain, and J. W. P. Hsu, Appl. Opt. **37**, 84 (1998).
[70] N. D. Browning, S. J. Pennycook, M. F. Chisholm, M. M. McGibbon, and A. J. McGibbon, Interface Sci. **2**, 397 (1995).
[71] R. Feidenhans'l, A. Kazimirov, D. M. Smilgies, Q. Jiang, and J. Zegenhagen, Philos. Mag. Lett. **78**, 51 (1998).
[72] B. D. Huey and D. A. Bonnell (unpublished).
[73] G. Duscher (private communication).
[74] B. D. Huey, Ph.D. thesis, University of Pennsylvania, Philadelphia, 1999.